Reservoir monitoring: A multidisciplinary feasibility study

BIONDO BIONDI, GARY MAVKO, TAPAN MUKERJI, and JAMES RICKETT, Stanford Geophysics Department
DAVID LUMLEY, Chevron, La Habra, California
CLAYTON DEUTSCH, University of Alberta
RUNAR GUNDESØ, Norsk Hydro
MARCO THIELE, Stanford Petroleum Engineering Department

There is a recognized need to combine the skills of geoscientists and engineers to build quantitative reservoir models that incorporate all available reservoir data. These integrated models are critical for forecasting, monitoring, and optimizing reservoir performance because they will enable more accurate flow simulation studies, identification of permeability flow paths and barriers, mapping of bypassed oil, and monitoring of pressure and saturation fronts.

Available reservoir data include conceptual geologic models, seismic, cores, well logs, and production. Each carries information, at different scales and with varying levels of uniqueness, related to the true distribution of petrophysical and fluid properties. The challenge is to integrate all these disparate data into a unified, self-consistent reservoir model. Such a challenge can be tackled only via collaboration by specialists in the different disciplines.

This paper reports on a joint modeling effort among four research groups in the Stanford School of Earth Sciences: Stanford Center for Reservoir Forecasting; Stanford University Petroleum Research Institute (Reservoir Simulation); Stanford Rockphysics and Borehole Geophysics Project; and Stanford Exploration Project. Our approach in the work reported here was to involve all of the groups in a more systematic way and at all levels of the project.

Background. The starting point was building a model (Figure 1) whose lithology and structure resemble a North Sea reservoir. We then simulated three years of multiphase fluid flow and production history, and estimated the effective seismic responses caused by various combinations of the lithologic model and the fluid properties. Finally, we simulated multioffset 3-D seismic surveys at different times during production.

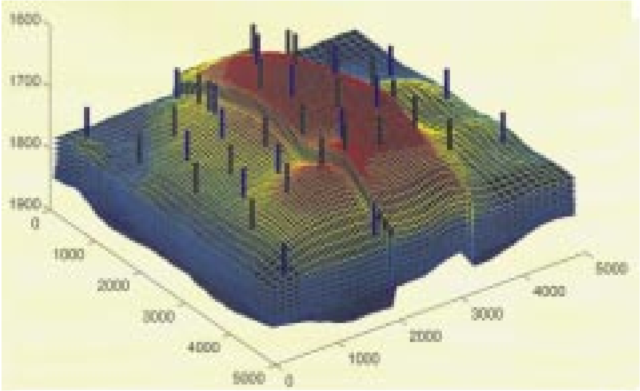

Figure 1. The reservoir model, showing structure and faults. The lithology was fashioned after braided stream fluvial reservoirs common in many parts of the world, including the North Sea. Production wells are black; injection wells are blue.

While the macroscale of our model reservoir is constant (5×5 km), the sampling of the reservoir physical parameters varies greatly between steps. The main scales that we used are described below.

The core scale is about 0.1×0.1×0.1 m. Much of what is known about rock physics relations among rock, fluid, and seismic properties has come from measurements at the core scale. Description of the complete reservoir at this scale would yield 10^{13} (10 000 billion) voxels and is not practical. Nevertheless, in any reservoir, a subset of core data can yield seismic-to-reservoir properties relations that are critical to the seismic modeling.

The reservoir geological modeling scale is nominally 5.0 × 5.0 × 0.5 m. Ideally, the geologic model would be at the resolution of the best information, i.e., the core data.

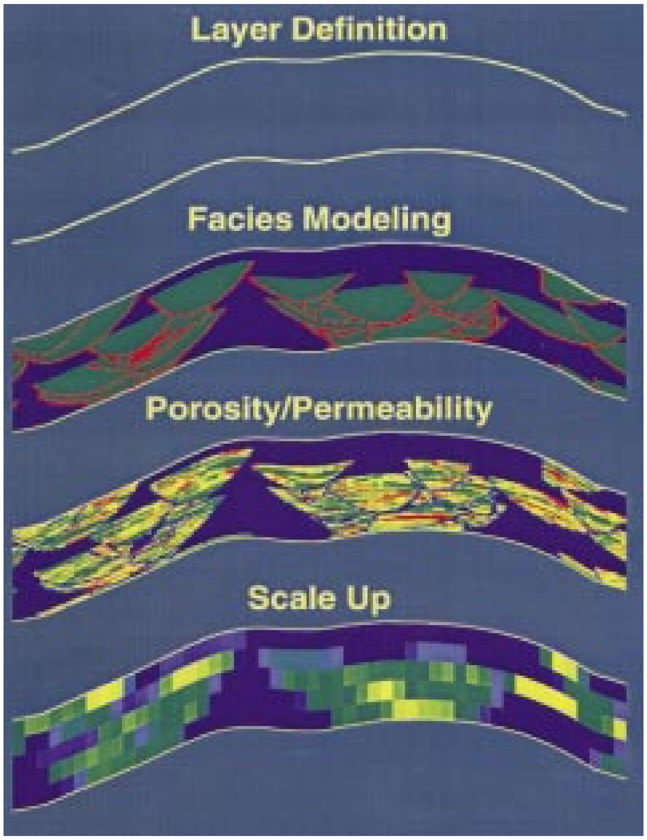

Figure 2. The steps in constructing the numerical reservoir model (from top to bottom): layer definition; object-based channel modeling; cell-based porosity and permeability modeling; and scaling-up to a resolution for flow simulation.

This is not practical and, instead, a scale is chosen small enough to capture the significant geologic heterogeneities and large enough to yield a tractable number of cells or voxels. The scale chosen here yields 200 million voxels, which is ambitious but practical for reservoir modeling. There are about 50 000 core scale voxels within a geologic modeling cell.

The scale of the grid blocks in fluid-flow simulation is a compromise between the desire to minimize artificial numerical artifacts, accounting for sufficient geologic and fluid flow details, and available computational resources. Full-field simulation (requiring 100 grid blocks between wells) can easily lead to systems with 10^6–10^8 grid blocks—well beyond current computational possibilities. In this study, a discretization of the macroscale into nx = 132 × ny = 140 × nz = 12 resulted in grid blocks with an areal scale of 62.5 × 62.5 m in the coarse region and 31.25 × 31.25 m in the refined region. The vertical size of the grid blocks, on average, was 8.3 m.

The seismic imaging scale is the scale of the resolution of the seismic images; this is linked with the wavelength of the signal recorded at the surface (50 m in our model). We described the seismic properties of the reservoir on a 5×5×5 m scale. Description at this scale of the whole reservoir would yield about 50 million voxels. We used a subset of the whole reservoir, about 1.5 million voxels.

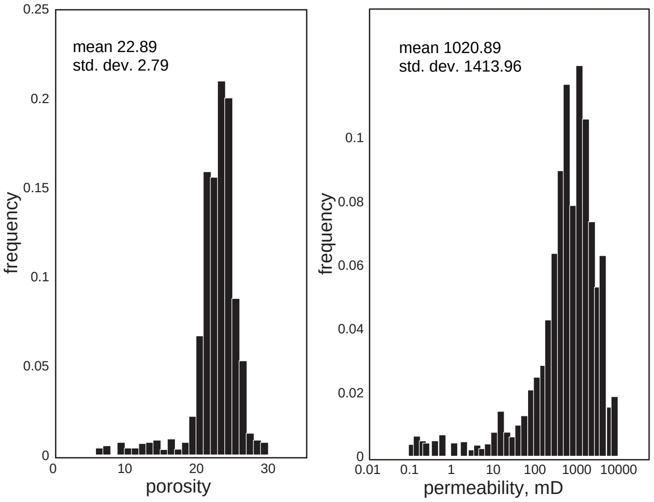

Figure 3. Histograms of porosity and permeability within channel sand.

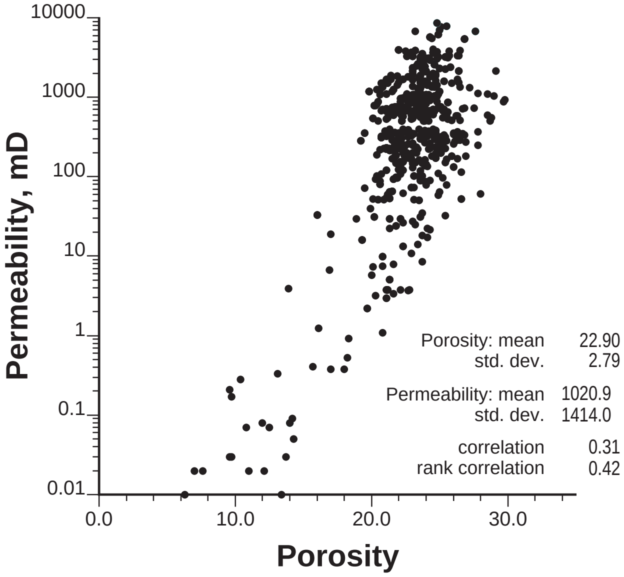

Figure 4. Porosity and permeability within channel sand.

Geologic modeling. A numerical geologic model of a braided stream fluvial reservoir with an average net-to-gross ratio (proportion of channel sand) of 0.65 was constructed with no well or seismic conditioning data. The model has 200 million cells and physical dimensions of 5 km in the *x* and *y* directions and 100 m in the *z* direction.

The vertical cell size is nominally 0.5 m; however, it varies areally to accommodate variation in the thickness from 80 m to 120 m.

High-resolution sequence stratigraphy, made possible by dense 3-D seismic and close-distance well logging data, reveals a framework of repetitive strata bounded by time-correlatable or chronostratigraphic surfaces. These strata often contain facies that contrast drastically in petrophysical properties such as permeability and porosity. It is necessary to treat these surfaces as first-order heterogeneities for reservoir description and fluid-flow modeling. In this modeling, the 100 m vertical extent was modeled with three geologic strata with net-to-gross ratios (proportion of channel sand) of, respectively, 0.8, 0.4, and 0.6. The top panel of Figure 2 shows a cross-section through one layer.

Once these strata are identified, the distribution of channel complexes versus overbank deposits within each layer represents second-order heterogeneities. The distribution of individual channels within each channel complex constitutes third-order heterogeneities. Sequence stratigraphy allows such hierarchical classification of het-

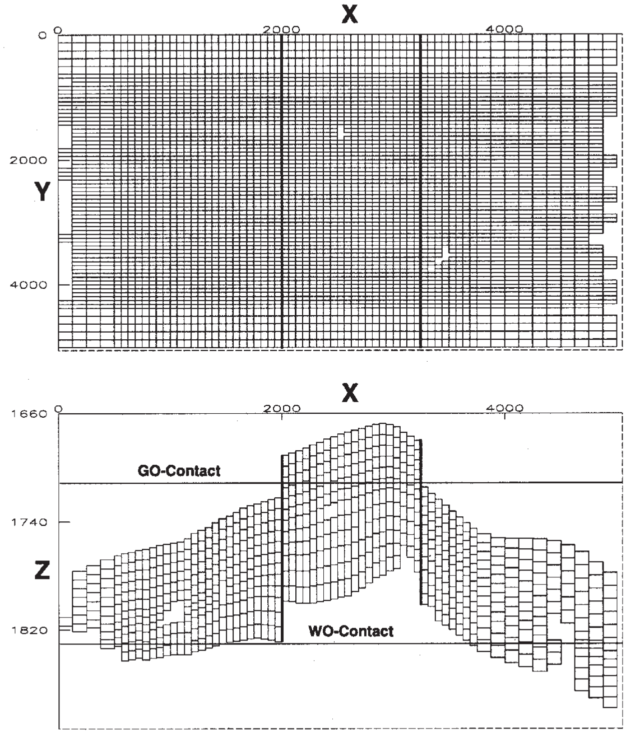

Figure 5. Areal and cross-sectional (y = 2270 m) meshing of the 50 674-cell model, showing locations of faults and the gas-oil and water-oil contacts. The larger, 202 696-cell model was constructed by doubling the number of grid blocks in the *x*- and *y*-directions.

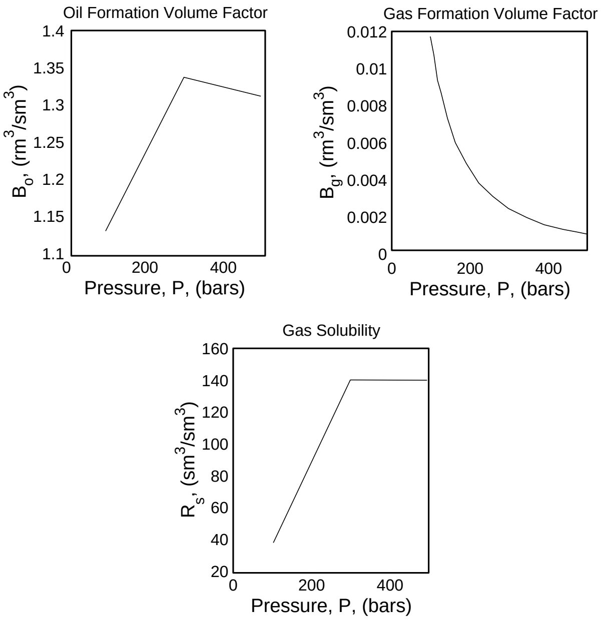

Figure 6. Oil and gas formation volume factors and gas solubility as a function of pressure. Solubility of oil into the gas phase was assumed zero. The water component is assumed present in the water phase only.

erogeneities down to the bed set or bed level. This genetic hierarchy of heterogeneities is best modeled through a hierarchical procedure. In this study, a hierarchical object-based procedure was applied to model the channel-sand distribution in each layer. The key geologic input parameters are: (1) the proportion of channel sand that could vary vertically and areally; (2) geometric parameters defining the channel thicknesses, widths, and sinuosities; and (3) well data. In this case, the layer proportions were assumed constant, realistic channel geometries were considered, and no well data were used to constrain the model. The second panel of Figure 2 shows a cross-section through the channel and overbank shale facies model.

A constant porosity of 15% and permeability of 0.01 mD were assigned to the overbank shale deposits. Although the total porosity of the overbank shales was 15%, the effective porosity was 0%. Within the channel sands, porosity was assigned with sequential Gaussian simulation (SGS). The SGS algorithm constructs a stochastic porosity model constrained to a histogram of porosity, a model of spatial correlation, and well data. Realistic input statistics were chosen on the basis of published North Sea examples. The third panel of Figure 2 shows a cross-section through the porosity model.

Finally, permeability was related to porosity through a scatterplot. Figures 3 and 4 give the histograms and porosity-permeability scatterplot.

The flow simulation blocks for the 200 000-block model are approximately 1000 times larger than the geologic model. The details in the model provide the ground truth petrophysical properties and are transferred to flow simulation as effective block properties. The scaled-up porosity was taken as the arithmetic average of the constituent porosity values (the fourth panel of Figure 2 shows a cross-section through the scaled up porosity model); the scaled-up horizontal permeability was taken as the arithmetic average of the constituent permeability values, and the scaled-up vertical permeability was taken as a power average of the constituent permeability values. This power average for the vertical permeability takes into account that the flow paths are more tortuous in the vertical direction because of lateral continuity.

Fluid-flow simulation. All fluid-flow simulations were done using the 1996A version of Eclipse, a three-phase, three-dimensional, general purpose black-oil simulator

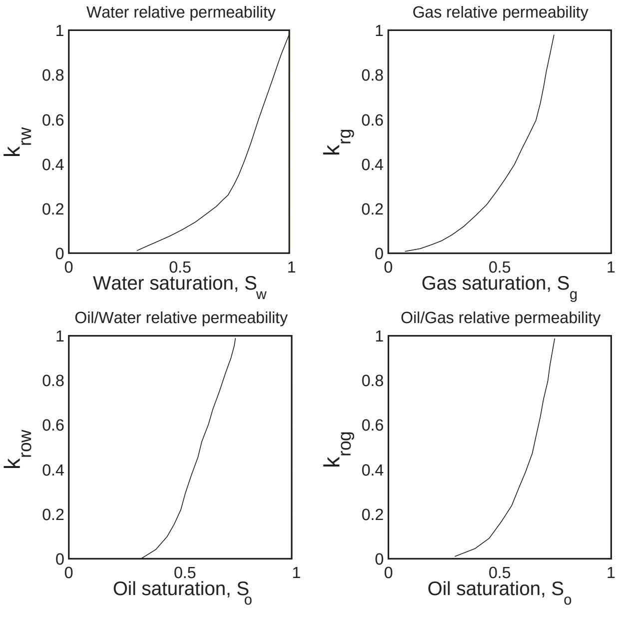

Figure 7. Relative phase permeabilities from a real North Sea data set used for the fluid-flow simulations.

from GeoQuest. *Black oil* is a term used to describe a set of simplifying assumptions used for modeling hydrocarbon phase behavior, in which all components are lumped into two pseudocomponents, oil and gas. Unfortunately, the words *gas* and *oil* are also used to distinguish between the vapor and liquid phase, sometimes confusing the uninitiated reader. Water is usually present as a third component and phase. The bulk of fluid-flow simulations in the industry are done using the black-oil model.

Two models were simulated. The first consisted of nx = 66, ny = 70, and nz = 12 grid blocks (50 674 active cells). In the second, the number of blocks in the *x* and *y* directions was doubled to nx = 132 and ny = 140. The number in the vertical direction was kept at nz = 12, resulting in 202 696 active cells. (Active cells are those with a porosity greater than 10^{-6}.) Results of the second model were used in the seismic processing. Both models were gridded using a Cartesian geometry, with a denser grid at the cen-

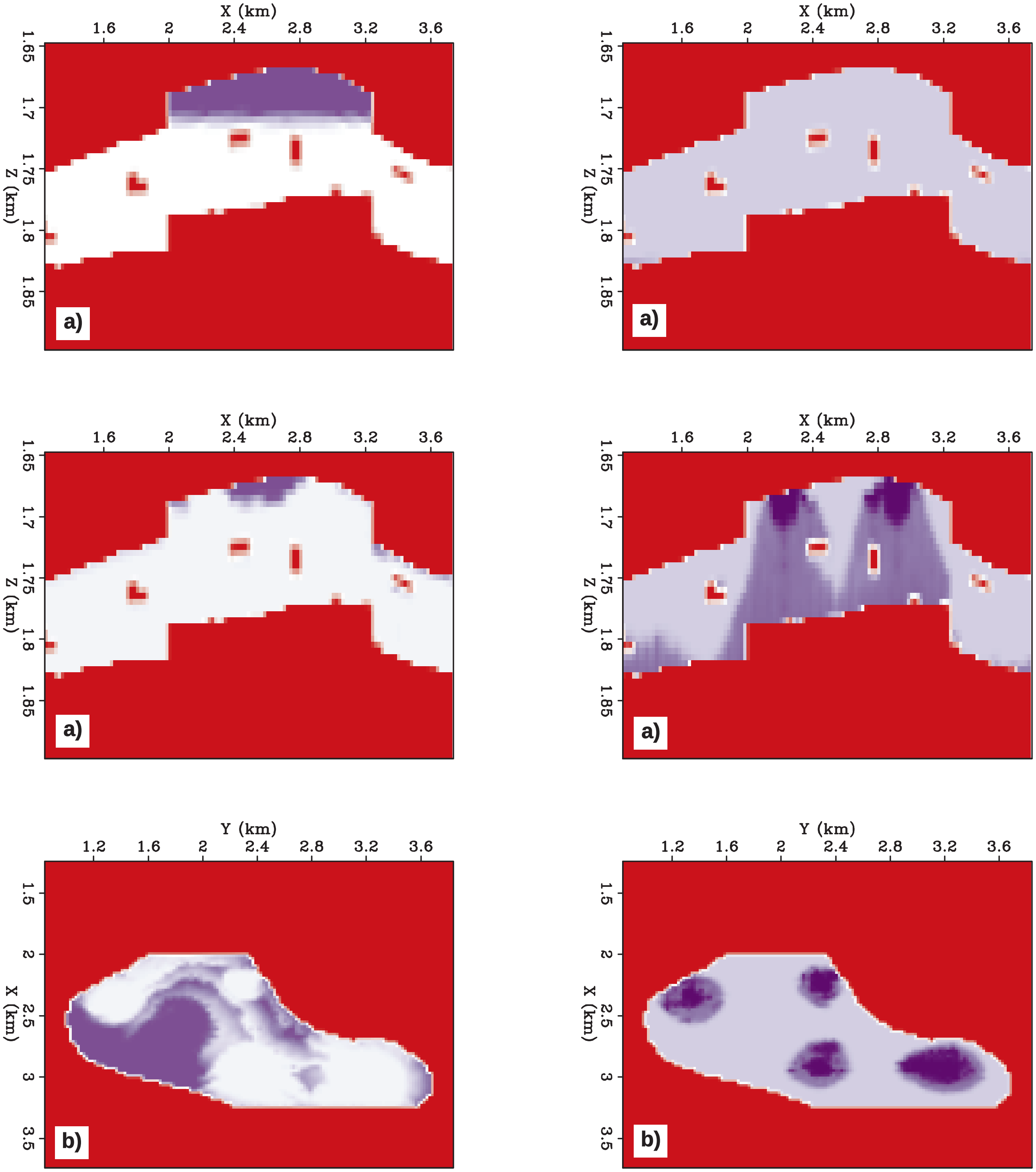

Figure 8. Gas (left) and water (right) saturation figures. (a) Vertical slice at 2.27 km, at t_0 (top), and three years later, t_1 (middle). (b) Horizontal slice at 1.69 km showing the reduction of the gas cap through pressure maintenance by the water injectors (white low saturation).

ter (Figure 5). The simulated area was 5×5 km; thickness varied between 80 and 120 m.

Two vertical faults, with an offset of 30 m, were introduced in the *yz*-plane. The faults were located at 1812.5 m and 3375 m. To account for the proper connections across the faults, 1260 nonneighbor connections were introduced in the 50 674-cell model and 2520 nonneighbor connections in the 202 696-cell model. Nonneighbor connections are required when blocks which are neighbors in the *i,j,k* ordering used as input are not neighbors in the actual physical space (as, for example, in the case of faults). Transmissibilities across the faults were then multiplied by 10 (at 1812.5 m) and by 10^{-5} (at 3375 m), thereby increasing the transmissibility of the first fault while almost sealing the second fault. Figure 5 shows the areal view of the top layer and a *xz*-slice at $y = 2270$ m.

Properties for the simulations were picked to resemble a North Sea oil. Formation volume factors for oil and gas as well as the solubility of the gas component into the oil phase are shown in Figure 6. The oil component was assumed to be present in the oil phase only.

The effective permeability of the rock to a phase is taken as the product of the absolute permeability times the relative permeability of the phase which is a function of saturation. Relative permeabilities used in the simulations are shown in Figure 7, and were taken from a North Sea data set. Relative permeabilities for water and gas are assumed to be a function of their own saturations only.

Simulation. The initial conditions included a datum pressure of 300 bars at the gas-oil contact at a depth of 1710 m. The water-oil contact was at 1830 m.

The reservoir was produced under primary production for the first six months with 24 production wells producing at 5000 m^3/d and a minimum bottom-hole pressure constraint of 200 bars. After this, 17 wells injected water at 5000 m^3/d with a maximum bottom-hole pressure constraint of 400 bars. The total simulation time was three years. Only vertical wells were included.

Example fluid distributions at three years for a vertical cross-section and a horizontal slice are shown in Figure 8. Water injection has clearly reduced the size of the gas cap and is seen to be influenced by gravity, as shown by the conelike pattern around the injection wells.

Table 1 summarizes performance data for the simulations.

Table 1. Memory use and CPU times for the fluid flow simulations.

Models	66 ¥ 70 ¥ 12	132 ¥ 140 ¥ 12
Memory	122 MB	441 MB
Simulation time	3 years	3 years
Volume produced	0.248 pore volumes	0.246 pore volumes
CPU time (1)	2.2 hr	71.0 hr
CPU time (2)	1.1 hr	—
CPU time (4)	0.71 hr	—
CPU time (8)	0.40 hr	—

Rock physics modeling. Rock physics links reservoir properties and the seismic properties observed with a geophysical survey. The important parameters are lithology, porosity, permeability, pore fluid types and saturations, temperature, reservoir effective stress, and pore fluid pres-

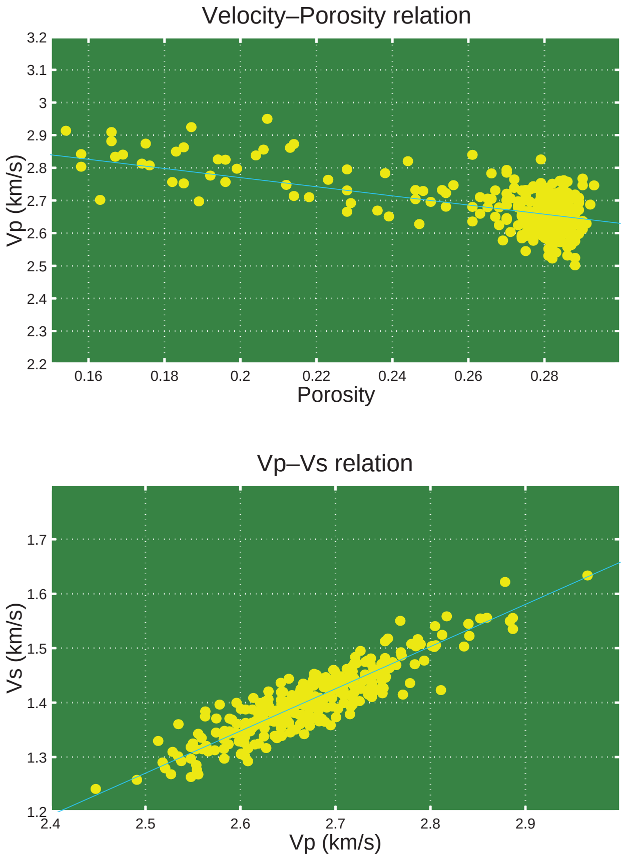

Figure 9. Velocity-porosity and $V_p - V_s$ regressions representative of North Sea reservoirs used to define the reference rock properties.

sure. The related bulk properties that most impact seismic wave propagation are bulk density, and *P*- and *S*-wave velocities.

Bulk density is the easiest to understand and quantify. Density is the simple volumetric average of all mineral (solid) and pore fluid (solid, liquid, and gas) phases in the rocks. Density changes during reservoir production are primarily the result of replacing the initial set of fluids with another set.

Seismic velocity is related to the ratio of elastic stiffness of the fluid-bearing rocks to the bulk density of the rocks. The elastic stiffness depends on the mineralogy, the stiffness of the pore space, and the stiffness (incompressibility) of the mixture of pore fluids in the rock. This is most effectively quantified with the well-known Gassmann's equation, which relates the bulk modulus of the saturated rock to the dry rock bulk modulus, the mineral modulus, the fluid incompressibility, and the porosity.

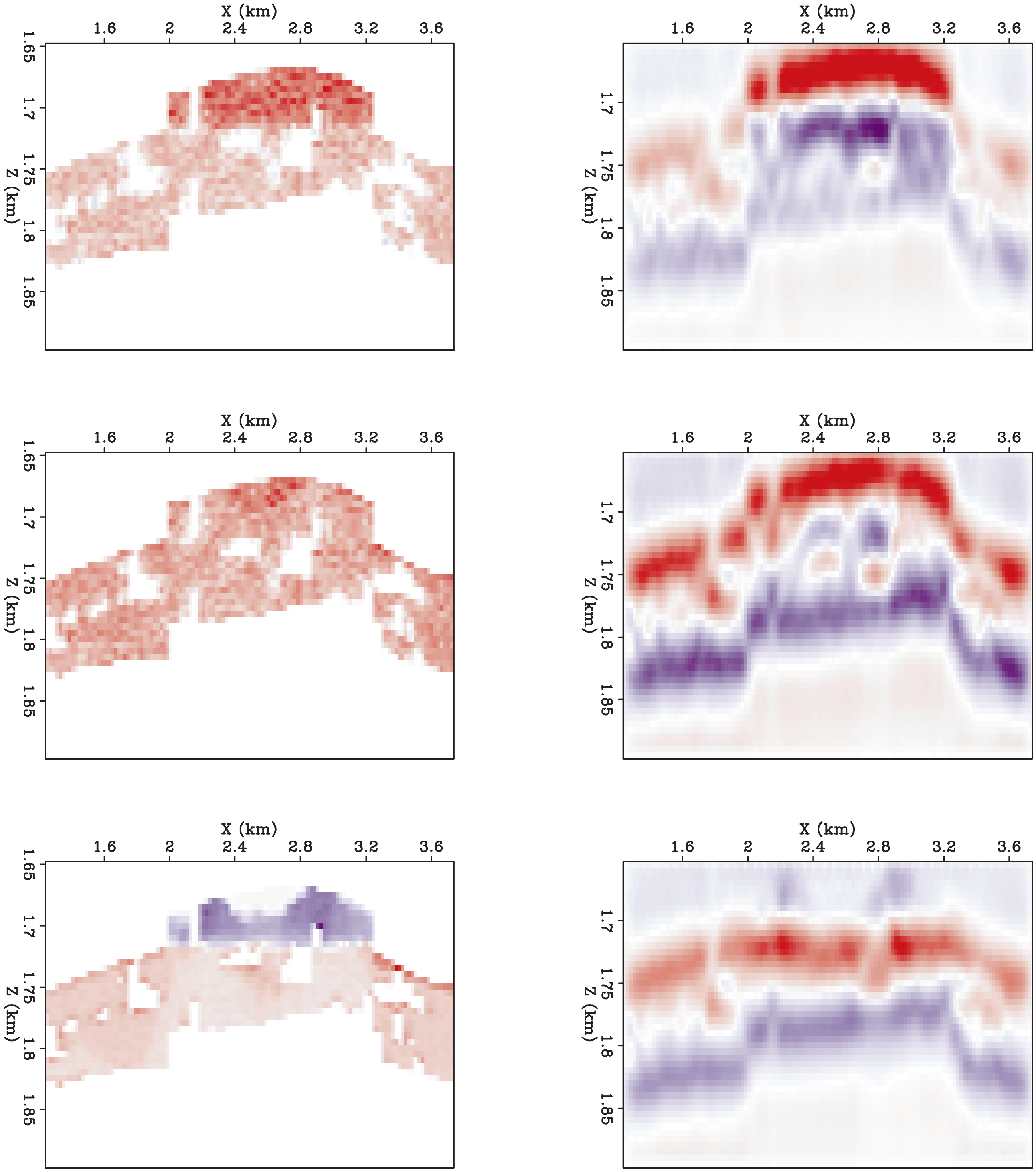

a)

b)

Figure 10. Vertical slices at cross-line 2.27 km. Left panels show acoustic impedance model; right panels show the results of seismic imaging. Top row is at t_0, middle row is at t_1, and bottom row is their difference.

Important issues when doing fluid substitution include:

- Frequency: Gassmann's relation is most appropriate for very low frequencies as used in surface seismic. At higher frequencies as used in laboratory ultrasonic and sonic log measurements, fluid effects can give rise to velocity dispersion. This has to be taken into account when using velocity-porosity regressions obtained from high-frequency data. The amount of velocity dispersion depends on the nature of the pore space compressibility. It is enhanced in the presence of soft cracklike pore space, and decreases at high effective pressures when most of the cracklike porosity in closed.
- Saturations and heterogeneity: The effective elastic stiffness of the rock depends on the saturation (among other things), and also on how the saturation is distributed within the pore space. A saturation distribution that is homogeneous and uniform at the pore scale within each grid block will give a different velocity than a heterogeneous saturation. The two situations require different mixing rules to estimate the effective seismic velocity. For the present exercise, the saturation was taken to be

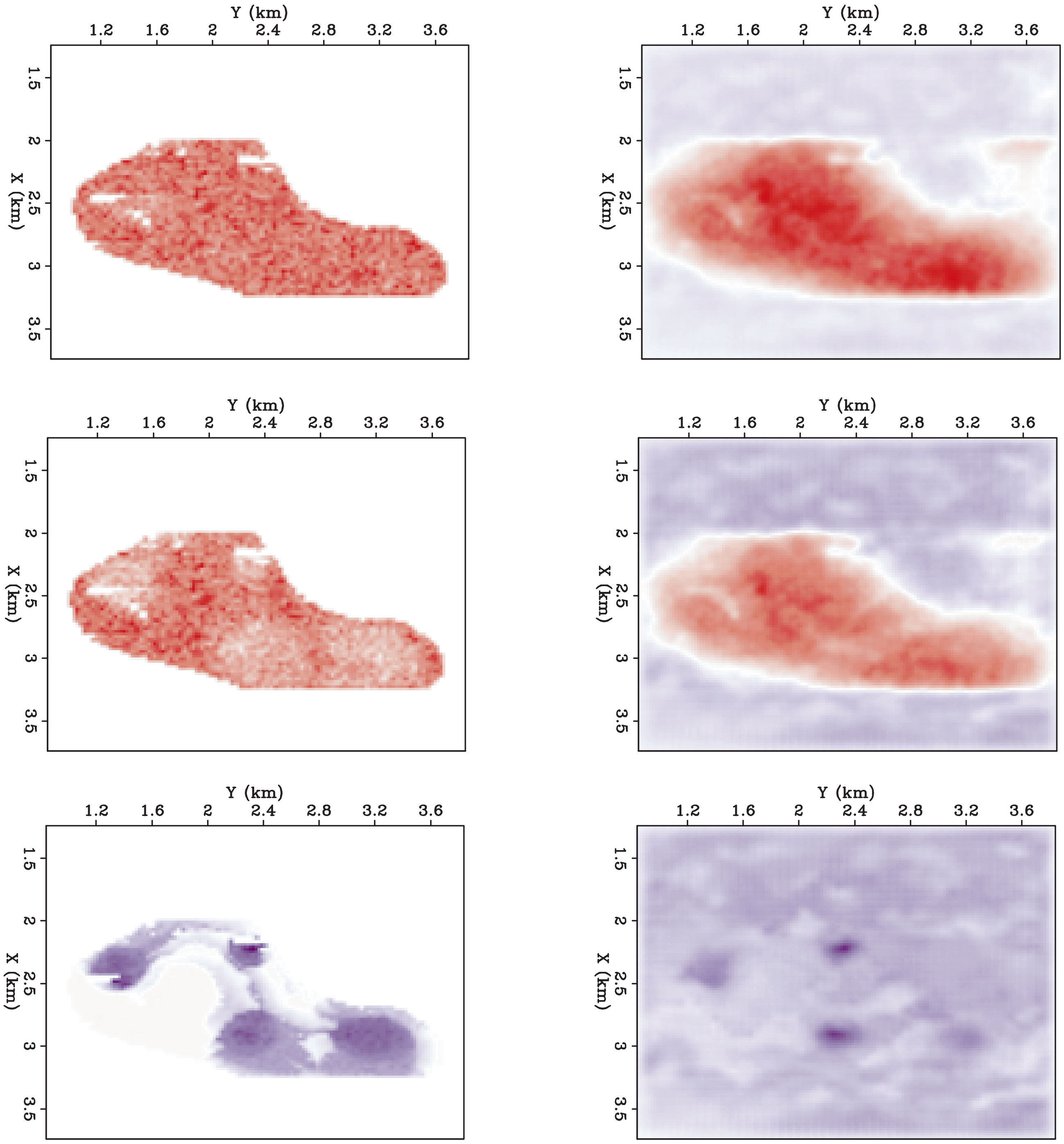

a)

b)

Figure 11. Horizontal slices at 1.690 km. Left panels show acoustic impedance model; right panels show the results of seismic imaging. Top row is at t_0, middle row is at t_1, and bottom row is their difference.

homogeneous within each grid block, and an effective fluid incompressibility (calculated as the Reuss or harmonic average of the individual fluid incompressibilities) was used in Gassmann's equation.

The fluid densities and incompressibilities used in the modeling were obtained from the empirical relations of Batzle and Wang (1992) as incorporated in PetroTools, a seismic rock properties software by PetroSoft.

Velocity-porosity regression. Laboratory and sonic log measurements show that velocities usually decrease with porosity, though the velocity-porosity relations are not always unique. *P*- and *S*-velocities are also often well correlated. Velocity-porosity and $V_p - V_s$ regressions have been presented in the literature for different lithologies. We used similar regressions (Figure 9) to define a reference V_p, V_s, and density. For the sand facies, we choose a VP-ϕ regression of the form V_p (km/s) = 3.05 – 1.4ϕ with a coefficient of variation around the regression of about 2.4%. The $V_p - V_s$ regression was V_s (km/s) = 0.775 V_p – 0.67, with about 2% coefficient of variation. These are representative of typical water saturated sands from North Sea fields. The regressions (along with the spreads around the regressions) were used to generate the reference V_p and V_s data. We did not include the effect of pressure variations on the regressions, though the effect of pressure on the fluid properties was taken into account. The reference velocities were transformed, applying Gassmann's equations, to the reservoir conditions using the pressure, saturations, and gas-oil ratio obtained from the flow simulator. This was done at each time step of interest in the production history. The fluid incompressibilities and densities as a function of pressure and gas-oil ratio were calculated from published laboratory relations. For the shale facies, which was assigned a zero effective porosity and negligible permeability, we assigned fixed V_p, V_s, and density of 2.5 km/s, 1.3 km/s, and 2.27 gm/cc, respectively.

One task involved mapping the flow-simulator output onto a regular Cartesian grid appropriate for seismic modeling. The flow-simulator results are defined on a stratigraphic coordinate system with variable block sizes, usually larger than the seismic blocks. The porosity (which is defined at the geologic model scale) is also on an irregular stratigraphic coordinate system but with blocks smaller than the seismic scale. For upscaling the porosity to the seismic scale, a simple volumetric block averaging was used. The flow simulator outputs were downscaled to the seismic blocks by linear interpolation, first along the depth direction, and then in each horizontal layer. This highlighted the need for better methods of upscaling the rock and reservoir properties, and also for better relations between the rock physics and the seismic data.

Seismic modeling and imaging. Since, in this case, the seismic modeling required a technique that could handle a model that is both elastic and heterogeneous, our choice of method was restricted.

Zoeppritz or reflectivity methods can model only homogeneous plane layers and cannot capture the effect of heterogeneities. Finite-difference or spectral methods are too computationally intensive for modeling a full multioffset 3-D survey. This suggested a ray-based scattering approach, such as the first-order Born approximation as described by Wu and Aki (1985). More detailed description of the modeling method and direct comparison with the Zoeppritz method can be found in Rickett et al. (1996).

Two seismic surveys were computed over a 2×3 km central block of the modeled reservoir. The first (t_0) was recorded at the beginning of production, and the second (t_1) after three years of production (which included $2^1/_2$ years of water injection). The data sets covered the reservoir with 30-m spacing between common midpoints in both directions. Each data set contains two different offsets (source-receiver distance): zero offset and 3-km offset. Multioffset surveys allow the analysis of amplitude vari-

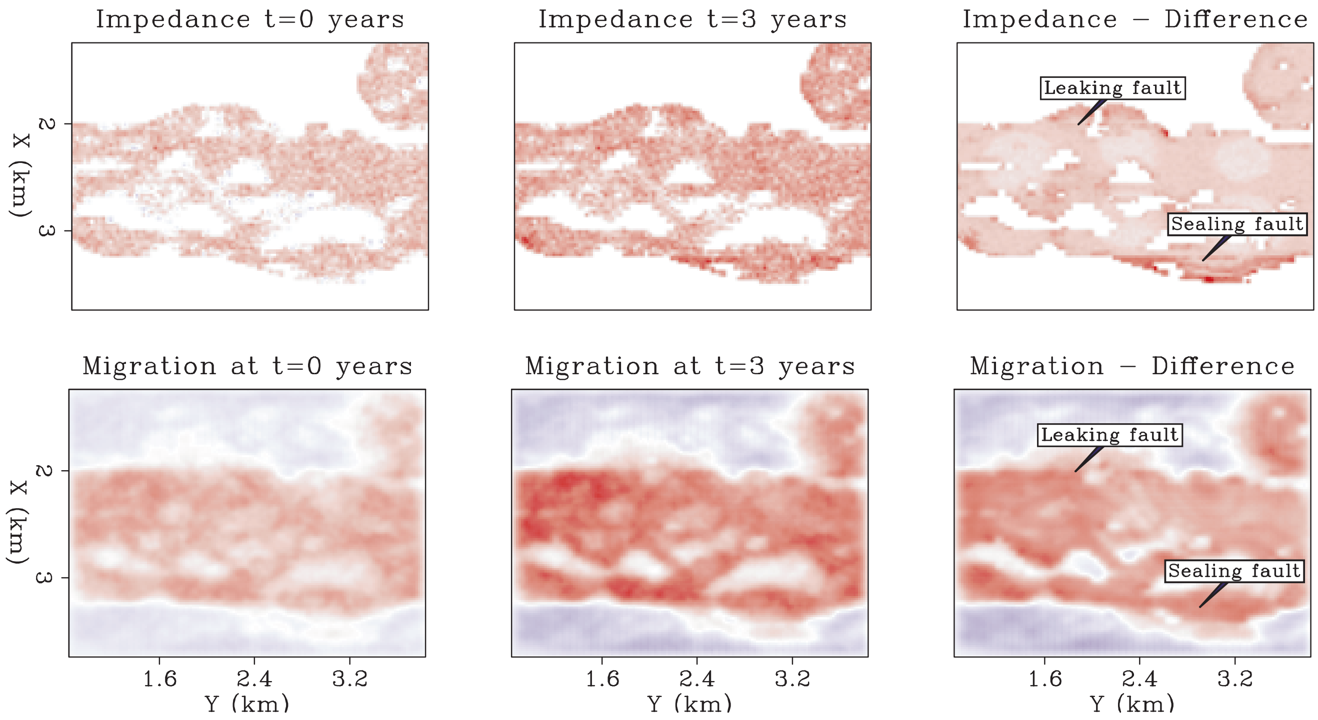

Figure 12. Horizontal slices at 1.725 km. Top panels show acoustic impedance model; bottom panels show the results of seismic imaging. Left column is at t_0, middle column is at t_1, and right column is their difference.

ation with offset (AVO), which can be useful for identifying variations in the fluid type. The background velocity function was linearly increasing with depth, starting from a velocity of 2 km/s and a constant gradient of 0.28 s^{-1}.

The wavelet used in the modeling had a maximum frequency of about 45 Hz, giving a wavelength of about 50 m in the target. This is reasonable, but a lower limit on the resolution expected for a target of this depth. Further modeling will be done with higher frequencies.

The modeled data was imaged using a Kirchhoff 3-D prestack migration program. The kinematics and amplitudes used by the migration were obtained by numerically tracing rays through the given background velocity function. The migration code had the appropriate antialiasing corrections and amplitude tapering to preserve the correct amplitudes. The different offsets (0 and 3 km) in the data sets were migrated and analyzed separately.

Monitoring results. The seismic imaging results from the zero-offset data will be presented side by side with the cor-

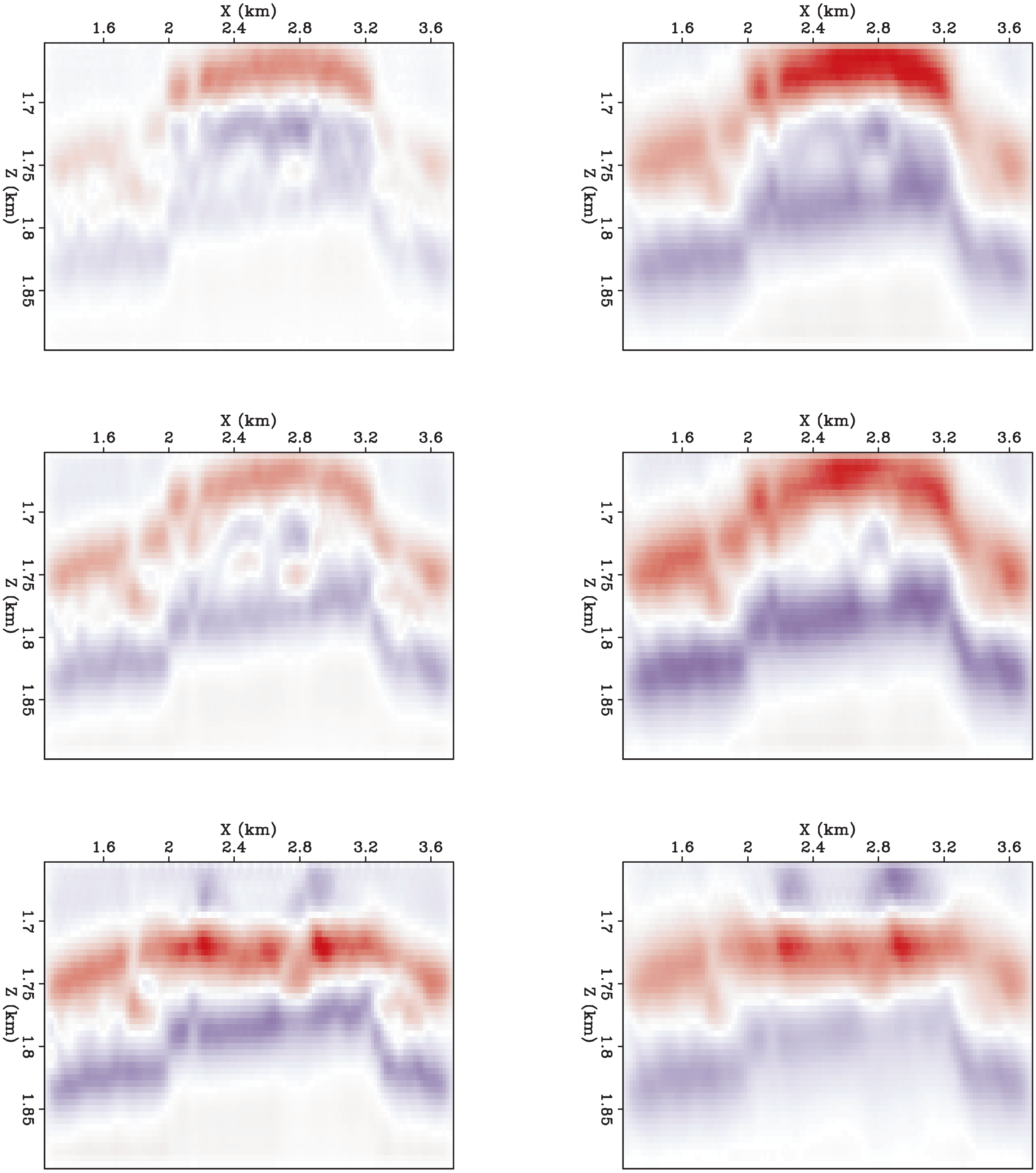

Figure 13. Vertical slices at cross-lines 2.27 km. Left panels show the result of imaging the zero-offset surveys; right panels show the imaging of the 3-km offset surveys. Top row is at t_0, middle row is at t_1, and bottom row is their difference.

responding seismic effective properties used as input to the modeling and imaging procedure. To enable direct comparisons, we show sections through the acoustic impedance cube and through its estimates derived from the seismic migration results. These impedance estimates were obtained by integration along the depth axis of the migration results.

Figure 10 shows vertical sections through the acoustic impedance cube taken at cross-line 2.27 km where two water-injecting wells were located. The sections on the top show the "impedance" values at t_0, while the sections in the middle show the values at t_1. The bottom sections show the values at t_0 subtracted from the values at t_1. The effects of the water injection, which causes the gas cap to be unevenly depleted, are apparent.

The spatially heterogeneous nature of the gas-cap depletion is also evident from the horizontal slices (at a depth of 1.69 km) in Figure 11. These correlate very well with the images showing the gas saturation and water saturation (Figure 8). The relative low frequency and, consequently, low-resolution of our surveys prevents the migration from imaging the spatial heterogeneities at the same level of detail in the seismic impedance model. This observation confirms that reservoir monitoring does indeed require advanced seismic acquisition and processing technologies aimed at maximizing the resolution of the final seismic images.

Figure 12 shows horizontal slices from deeper in the reservoir (1.725 km). The effects of the formation of a small gas cap on the side of the sealing fault are apparent in both difference sections. The formation of this gas cap can be seen also in the vertical slice through the gas saturation field (Figure 8) and the vertical slice through the seismic properties (Figure 10). Another apparent feature of these horizontal slices is the low-permeability shale bodies. These areas show very low values in the difference section, since low permeability prevents large changes in fluid properties and are potential barriers to fluid flow.

Figure 13 shows the potential additional information that can be obtained from imaging nonzero offset data. It shows the same sections from the right side of Figure 10 with the equivalent section from the migration of the 3-km offset data. As expected from migration theory, the results from nonzero offset data (right side of Figure 13) have lower resolution than those from zero-offset data (left side of Figure 13). However, beside this resolution mismatch, the variations with offset in the seismic response of gas-saturated sand is apparent. These differences are mostly visible at t_0 when the gas cap was not depleted, and in the difference section in which the effects of the water-injecting wells are enhanced.

The results of the seismic imaging and modeling suggest that fluid-flow patterns and variations of fluid properties within the reservoir can be detected using 3-D seismic. However, conclusions should be drawn cautiously from these results since they were not affected by all the factors that in a real case would degrade the results (e.g., noise, acquisition constraints, and uncertain knowledge of the overburden parameters).

Future considerations. The goal of this project was to begin a collaborative effort between various disciplines, which included geologic reservoir modeling, fluid-flow simulation, rock physics, and seismic imaging to explore and understand how reservoir monitoring may be used for efficient reservoir management. Seismic monitoring promises to provide valuable information about fluid movements and geologic heterogeneities. However, issues of resolution, scales, and uncertainties need to be explored.

Our preliminary results warrant further research. Future work has begun to address:

- Using seismic monitoring to constrain geologic models and reduce uncertainty in forecasting reservoir performance. In the context of stochastic reservoir modeling, flow simulation is performed with alternative, equally probable geologic models. The uncertainty in future performance is measured by the differences in flow simulation outcomes. The information provided by seismic monitoring will possibly reduce this uncertainty by constraining the models.
- In this study we performed the reservoir-to-seismic modeling flow on a single geologic realization. Future work should address the computationally challenging issue of using multiple geostatistical realizations. This will be feasible only if sufficient resources are available for the computationally intensive seismic imaging and fluid-flow simulations, and if efficient algorithms are developed to model the process with acceptable resolution at the relevant scales.
- Estimating uncertainties due to nonunique assignment of acoustic properties from the reference lithofacies, porosity, and saturations. Laboratory experience has demonstrated that seismic properties depend on pore fluid saturations, and also on the scales of their spatial distributions. The impact of this at field scales must be explored. This project highlighted the need for better methods of upscaling the rock and reservoir properties, and also the rock physics relations between these properties and the seismic observables.
- The essence of seismic monitoring is the capability for analyzing the differences between seismic images from data sets recorded at different times, with variations in acquisition geometry, waveform, bandwidth, and coherent noise. Methods to remove the effects of all these perturbations must be developed to enable seismic monitoring to reduce the uncertainties of reservoir characterization.

We envision that future work build on the multidisciplinary collaboration already started, consider real reservoir data, and provide fertile ground for applicable solutions to reservoir management problems. LE

S**uggestions for further reading:** "Seismic properties processing of pore fluids" by Batzle and Wang (GEOPHYSICS, 1992). *GSLIB (Geostatistical software library and user's guide* by Deutsch and Journel (Oxford University Press, New York, 1997). *Geostatistics for natural resources evaluation* by Goovaerts (Oxford University Press, New York, 1997). "Seismic monitoring of oil production: A feasibility study" by Lumley et al. (SRB 1994 annual report). *The rock physics handbook* by Mavko et al. (Cambridge University press, 1998). *The properties of petroleum fluids* by McCain (PennWell Books, Tulsa, 1990). "Four-dimensional seismology and (true) direct detection of hydrocarbons: petrophysical basis" by Nur (*TLE*, 1989). "Modeling heterogeneous reservoirs using the first order Born approximation" by Rickett et al. (SEP report, 1996). "Scattering characteristics of elastic waves by an elastic heterogeneity" by Wu and Aki (GEOPHYSICS, 1985).

Acknowledgments: We would like to thank Silicon Graphics for loaning a 16-processor Power Challenge that has been the main computational platform for the project. We also would thank GeoQuest for making Eclipse available and Jon Norris for installing and helping us run the code.

Corresponding author: T. Mukerji, mukerji@pangea.Stanford.edu